Green Chemistry

PAPER

View Article Online
View Journal | View Issue

Cite this: *Green Chem.*, 2025, **27**, 8300

Green solvent-based separation and regeneration of layered ternary cathode materials for sustainable lithium-ion battery recycling†

Liying Ou,‡[a] Ying Zhang, ‡[b] Pengwei Li, *[a] Kai Zhu, [a] Yinyi Gao[a] and Dianxue Cao *[a]

Direct regeneration serves as a promising approach for recovering layered ternary cathode materials. However, efficient separation of cathode materials from Al foil remains a key challenge for this approach. In this study, $LiNi_{1/3}Co_{1/3}Mn_{1/3}O_2$ (NCM111) is used as a model material, and a green separation strategy based on Hansen solubility parameters is developed. Using triethyl phosphate (TEP) to separate the cathode electrode sheets, the molecular structure of polyvinylidene difluoride (PVDF) is effectively destroyed at 110 °C, and the separation rate between the cathode material and the Al foil reached 94.1%. The separation mechanism is driven by hydrogen bond competition. Density functional theory calculations confirmed that TEP forms stronger hydrogen bonds with the –OH groups on the Al foil surface than PVDF, promoting its detachment. Additionally, TEP's high dielectric constant and solubility compatibility enhance PVDF dissolution. The recovered cathode material is regenerated using the eutectic molten salt method, with $LiOH–Li_2CO_3$ eutectic salt as the lithium supplement. The regenerated NCM111 exhibits excellent electrochemical performance, with a discharge specific capacity of 141.4 mAh g^{-1} at 1C and 86.9% capacity retention after 100 cycles. This TEP-based strategy provides a sustainable and efficient closed-loop recycling solution, offering new insights for the development of environmentally friendly battery recycling technologies.

Received 3rd April 2025,
Accepted 16th June 2025

DOI: 10.1039/d5gc01636c

rsc.li/greenchem

Green foundation

1. The innovative use of environmentally friendly solvent triethyl phosphate (TEP) achieves efficient removal of polyvinylidene difluoride (PVDF) binder with a separation rate of cathode materials up to 96%, no corrosion, and no toxic by-products, facilitating green battery recycling.
2. Based on the hydrogen bond competition mechanism and solubility parameter matching, TEP replaces harmful solvents, solves separation problems at the molecular level, and considers both recycling efficiency and environmental friendliness.
3. Through the low-energy eutectic salt method, the ternary cathode material can be efficiently repaired with performance close to that of commercial materials, a green closed-loop recycling system can be built, and the sustainable reuse of battery materials can be promoted.

1 Introduction

The rapid expansion of ternary lithium-ion batteries (LIBs) utilizing $LiNi_xCo_yMn_{1-x-y}O_2$ (NCM) cathodes has precipitated urgent demands for sustainable recycling infrastructure aligned with circular economy principles.[1,2] As the dominant power source for electric vehicles, these batteries deliver specific energies of 200–250 Wh kg^{-1} but face retirement within 5–8 years of service due to capacity fade below 80% initial performance.[3,4] The volume of decommissioned ternary LIBs in China is rapidly increasing and is expected to reach 160.4 GWh by 2030, posing a dual challenge: mitigating environmental risks caused by improper disposal while recovering strategic metals (Ni: 10–15 wt%, Co: 5–10 wt%, Li:

[a]*Key Laboratory of Superlight Materials and Surface Technology of Ministry of Education, College of Material Science & Chemical Engineering, Harbin Engineering University, Harbin 150001, China. E-mail: pengweili2024@hrbeu.edu.cn, caodianxue@hrbeu.edu.cn*

[b]*CAS Key Laboratory of Molecular Nanostructure and Nanotechnology, CAS Research/Education Center for Excellence in Molecular Sciences, Beijing National Laboratory for Molecular Sciences (BNLMS), Institute of Chemistry, Chinese Academy of Sciences (CAS), Beijing 100190, China*

†Electronic supplementary information (ESI) available. See DOI: https://doi.org/10.1039/d5gc01636c

‡These authors contributed equally to this work.

3–5 wt%).[5] Current recycling methodologies, however, exhibit critical limitations in preserving the structural hierarchy of layered oxide cathodes (commercially valued at 18–22 $ per kg) and preventing secondary pollution from fluorine-containing compounds during processing.

Conventional recycling technologies prioritize elemental recovery over material conservation, incurring substantial value loss. Pyrometallurgical approaches, operating at 1000–1200 °C, achieve 85–90% nickel and cobalt recovery but suffer >50% lithium volatilization while emitting 12–15 kg CO_2-equivalent per kilogram of processed batteries. Hydrometallurgical systems employing 2–4 mol L^{-1} sulfuric acid attain >95% metal dissolution efficiency but generate 8–10 L of acidic wastewater per kilogram cathode, requiring costly neutralization of fluoride ions (500–800 ppm) derived from PVDF binder decomposition.[6,7] More fundamentally, these methods induce irreversible structural degradation in NCM cathodes through complete dissolution of the $R\bar{3}m$ crystalline framework, yielding regenerated materials with compromised electrochemical performance (<140.0 mAh g^{-1} at 1C).[8] The technical bottleneck originates from the robust interfacial adhesion between PVDF binders and Al foil – a synergistic combination of hydrogen bonding and mechanical interlocking that resists conventional separation techniques.[9,10] Existing delamination strategies either thermally degrade PVDF above 450 °C (inducing LiF contamination and Al pitting corrosion) or rely on hazardous solvents like *N*-methylpyrrolidone (NMP) and dimethylformamide (DMF), which leave residual binder (>2 wt%) and compromise Al purity (<95%).[11–14]

To address the above challenges, researchers have proposed a variety of alternative separation strategies. Methods reported in the literature, such as the methanol–citric acid system,[15] deep eutectic solvents (DES),[16] aqueous cleaning systems,[17] and composite organic acid synergistic leaching systems,[18] have all demonstrated good separation performance and relatively low environmental impact. For example, the methanol–citric acid method achieves a separation efficiency of 99.5% after stirring at 45 °C for 15 min, avoiding metal loss. The organic acids used are biodegradable and environmentally compatible. DES systems (*e.g.*, choline chloride and ethylene glycol) can achieve nearly complete separation under mild conditions (120–190 °C), and are characterized by low toxicity and recyclability, making them a promising class of green solvents in recent years. In addition, aqueous sequential separation methods, by adjusting pH and using surfactants, can achieve non-destructive detachment of the cathode material and Al foil, offering simplicity, safety, and sustainability. Despite their respective advantages in greenness and separation efficiency, these methods still face challenges such as high solvent recovery costs, complex processes, and possible leaching of metal elements, which require further optimization.

In this study, we propose an eco-efficient delamination strategy utilizing triethyl phosphate (TEP) to address the long-standing challenge of separating cathode materials from Al foil in spent ternary LIBs.[19] This non-flammable organophosphate solvent selectively disrupts PVDF–Al foil interfacial interactions through competitive hydrogen bonding, where TEP's phosphate groups (P═O) and ethoxy groups ($-OC_2H_5$) preferentially bind to Al-OH sites over PVDF's F moieties. The process was run under mild conditions (110 °C, 120 min) and achieved 94.1% Al foil recovery while maintaining the integrity of the crystal structure of the cathode material $R\bar{3}m$. More importantly, TEP is a green solvent with low toxicity, low volatility, and recyclability. Throughout the separation process, no acid mist, no harmful HF gas, and no polluted wastewater are generated, truly achieving an efficient and environmentally friendly separation process. The regenerative NCM111 cathode provides an initial capacity of 141.4 mAh g^{-1} at 1C with a capacity retention rate of 86.9% after 100 cycles, comparable to commercial material performance (143.8 mAh g^{-1}, 89.1%). Demonstrating universal efficacy across high-nickel variants (NCM622/811), this methodology establishes a sustainable platform for direct cathode regeneration, bridging the gap between scalable recycling and high-value material recovery in the LIBs circular economy.

2. Experimental section

2.1 Materials and reagents

The spent LIBs used in this study are derived from BYD Co., Ltd, and their cathode active material composition is $LiNi_{1/3}Co_{1/3}Mn_{1/3}O_2$. The triethyl phosphate (TEP) solvent used was purchased directly from Shanghai Aladdin Biochemical Technology Co., Ltd and put into use without any pretreatment.

2.2 Experimental procedure

The cathode material with the electrolyte removed is designated as S-NCM. First, the disassembled electrode sheets were cut into small pieces and immersed in TEP solution at 110 °C, with stirring at a speed lower than setting 1 for 2 hours to achieve effective separation. Subsequently, the mixture was subjected to centrifugation to separate the solid material from the TEP solution under the following conditions: speed of 8000 rpm, and a duration of 25 minutes. The separated product was thoroughly washed with deionized water and dried at 60 °C, and then designated as D-NCM. Next, D-NCM was thoroughly mixed with two lithium sources (LiOH and Li_2CO_3) at a molar ratio of 5.25 : 1 using a planetary ball mill. Lithium supplementation and structural restoration were performed *via* the eutectic molten salt method, which involved a two-step calcination process. In the first step, the mixture was calcined at 450 °C for 5 hours in air to promote precursor reaction and preliminary structural reconstruction. In the second step, the temperature was raised to 850 °C and held for 12 hours to fully restore the crystal structure. The regenerated cathode material obtained through this process was named R-NCM. As a reference, the commercial cathode material was purchased from Guangdong Zhuguang New Energy Technology Co., Ltd and is referred to as C-NCM. The process

flow is shown in Fig. 1. Eqn (1) is used to calculate the recovery rate (η) of the NCM material.

$$\eta = \frac{m_2}{0.90 \times m_1} \times 100\% \quad (1)$$

where m_2 is the mass of the separated NCM, and 90% × m_1 is the theoretical mass of the NCM before separation. The original electrode composition is NCM : PVDF binder : conductive carbon = 90% : 5% : 5%.

2.3 Analysis and characterization

Functional group information of the material was identified using Fourier-transform infrared spectroscopy (FTIR; ALPHA II, USA) under the conditions of a resolution of 4 cm^{-1}, 32 scans, and a testing range of 400 to 4000 cm^{-1}. The crystal structure and its evolution were analysed using X-ray diffraction (XRD; max-TTRIII, Japan). The microstructure of the material was characterized by scanning electron microscopy (SEM; APREO SLOVAC, USA), while the nanostructure and lattice characteristics were further examined using high-resolution Transmission electron microscopy (HR-TEM; TECNAI F30, Japan), and the elemental composition of the cathode material was determined using energy-dispersive X-ray spectroscopy (EDS).

2.4 Electrochemical testing

The loading of the cathode active material is approximately 2.664 mg cm^{-2}, and the total electrode loading is about 3.33 mg cm^{-2}. The porosity of the regenerated material is 4.44% The assembly sequence of the CR2032 coin cell is as follows: anode case (CR2032), cathode electrode (12 mm in diameter), separator (16 mm), lithium foil (16 mm), spacer (16 mm), spring plate, and cathode case (CR2032). The electrolyte consists of 1.0 mol L^{-1} $LiPF_6$ in EC : DMC : EMC = 1 : 1 : 1 (v/v/v). The separator is a composite structure made of polyethylene (PE) and polypropylene (PP), with a thickness of 25 μm. The cycling performance and rate capability of the cells were tested using a Neware battery testing system (CT-4008). The tests were conducted at 25 °C within a voltage window of 2.8 to 4.4 V, with 1C corresponding to 180 mAh g^{-1}. Cycling performance was evaluated at 0.5C and 1C, while rate performance was tested at current densities of 0.1C, 0.2C, 0.5C, 1C, 2C, 0.5C, 0.2C, and 0.1C, with 5 cycles performed at each current density. Cyclic voltammetry (CV) was conducted at a scan rate of 0.1 mV s^{-1} within a voltage window of 2.8 to 4.4 V. Electrochemical impedance spectroscopy (EIS) was performed over a frequency range from 100 kHz to 0.01 Hz with an AC voltage amplitude of 5 mV.

2.5 Electrostatic potential and DFT calculations

The Multiwfn software combined with the VMD software was used to generate electrostatic potential maps on the most stable molecular surfaces of molecules or clusters with an electron density of 0.001 a.u. Density functional theory (DFT) calculations were performed using the VASP package with the projector augmented wave (PAW) pseudopotential and the Perdew–Burke–Ernzerhof (PBE) functional.[20,21] The program has a generalized gradient approximation of the projection-enhanced wave pseudopotential and Perdew, Burke, and Enzerh off (PBE) exchange correlation functions for optimizing the structure and obtaining the free energy of all structures.[22,23] To avoid periodic interactions, the vacuum

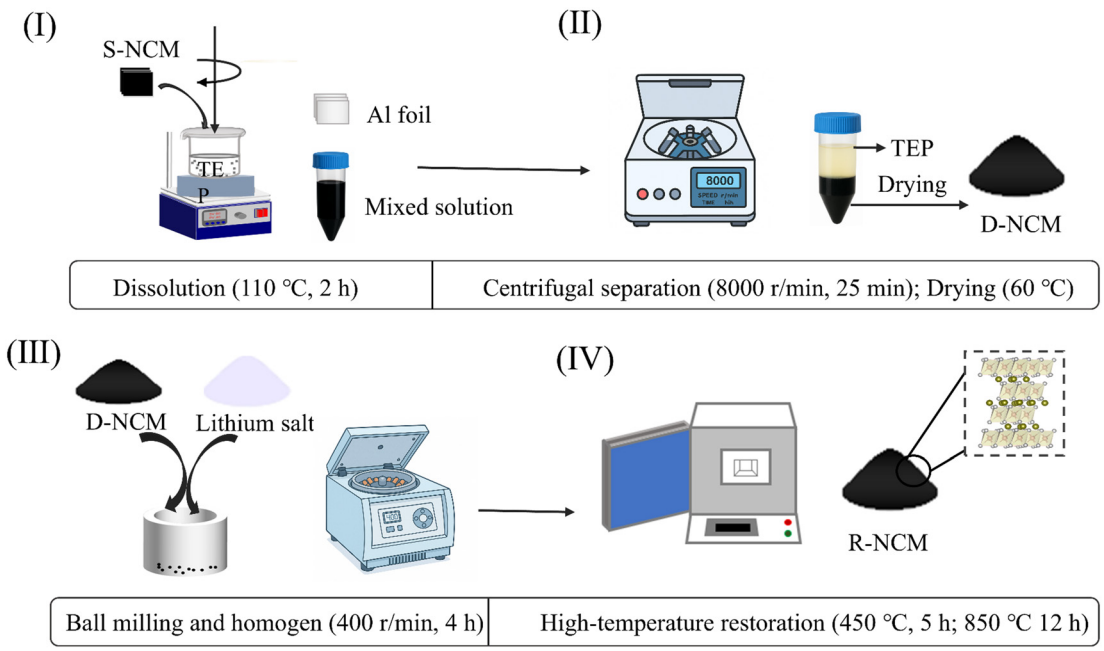

Fig. 1 Direct regeneration process flow chart: (I) Separation of NCM material and Al foil using TEP; (II) Centrifugal enrichment and drying of NCM material; (III) Mechanical ball-milling mixing of lithium salt and NCM; (IV) High-temperature calcination to reconstruct the crystal structure of NCM material, completing the regeneration and repair.

layer in the z-direction is set to 15 A. The cut-off energy of the planar wave basis set is 450 eV, and the adsorption energy is calculated using a 2 × 2 × 1 Monthorst encapsulated grid. The electron self-consistent iteration is set to 10^{-5} eV, and the positions of all atoms are completely relaxed until the residual force on each atom is less than 0.02 eVA^{-1}.

3. Results and discussion

3.1 Selection of separation solvent

Traditional electrode separation strategies focus on dissolving PVDF binders through HSP-guided solvent selection, where the three-dimensional parameter space (dispersive δ_d, polar δ_p, and hydrogen-bonding δ_h components) dictates dissolution efficacy.[24,25] The HSP distance (R_a) quantifies solvent-PVDF compatibility, with lower values indicating superior dissolution capacity. As revealed in Table 1, TEP demonstrates exceptional affinity with PVDF, exhibiting the lowest R_a value (1.1 $MPa^{1/2}$) among tested solvents. This stems from its optimal HSP alignment with PVDF (δ_d = 16.8 *vs.* 17.2, δ_p = 11.5 *vs.* 12.5, δ_h = 9.2 *vs.* 9.2), particularly matching the critical hydrogen-bonding component exactly. Comparatively, NMP shows moderate compatibility (R_a = 2.3) due to its δ_h deficiency (7.2 *vs.* PVDF's 9.2), while DMF's higher δ_h (11.3) introduces polarity mismatch (R_a = 2.4).[26,27] Notably, ethylene glycol (EG)'s extreme δ_h value (26.0) creates severe HSP deviation (R_a = 16.9), necessitating energy-intensive dissolution conditions. To evaluate the separation efficiency of different solvent systems under identical conditions (110 °C, 2 h) for spent NCM cathode materials, we compared the effectiveness of several solvents, as shown in Fig. S1.† It is evident from the figure that EG exhibits the weakest separation capability, being almost incapable of effectively detaching NCM material from the Al foil. Although NMP and DMF are able to achieve separation between the NCM material and Al foil, the process remains incomplete, which would significantly reduce the recovery rate of the NCM material. In contrast, the TEP-based separation method demonstrates excellent performance, achieving efficient separation of NCM material from Al foil. These experimental results are consistent with the predictions of the HSP model. Beyond solubility metrics, TEP's non-toxic nature contrasts sharply with NMP's recognized reproductive toxicity and DMF's hepatotoxicity, addressing both technical and environmental requirements simultaneously. This dual advantage positions TEP as a paradigm-shifting solvent that reconciles ultrahigh PVDF dissolution efficiency (R_a = 1.1) with green chemistry principles, overcoming the longstanding compromise between separation performance and environmental safety in battery recycling.[28]

Table 1 Hansen solubility parameters (δ_{di}, δ_p, δ_h) and compatibility distances (R_a) of PVDF and organic solvents

Compounds	δ_d $[MPa]^{1/2}$	δ_p $[MPa]^{1/2}$	δ_h $[MPa]^{1/2}$	R_a $[MPa]^{1/2}$
PVDF	17.2	12.5	9.2	—
NMP	18.4	12.3	7.2	2.3
DMF	17.4	13.7	11.3	2.4
EG	17.0	11.0	26.0	16.9
TEP	16.8	11.5	9.2	1.1

3.2 Characterization of the material and Al foil

Fig. 2a shows the SEM image of the untreated electrode, where the secondary particles of the cathode material are densely aggregated and firmly bonded to the Al foil due to the adhesive action of PVDF. This tight microstructure significantly increases the difficulty of separating the cathode material from the Al foil. Upon treatment with TEP solvent, the adhesive effect of PVDF is disrupted, resulting in the complete separation of the cathode material from the Al foil. Fig. 2b presents the SEM image of the recovered Al foil following this separation process. Fig. 2c and d further illustrates the change in the bonding state between the cathode material and the Al foil before and after TEP treatment. Fig. 2c shows the strong adhesion between the cathode material and the Al foil prior to treatment, while the Fig. 2d demonstrates the complete detachment of the cathode material from the Al foil after TEP treatment. Optical images further confirm the separation effect of TEP solvent, and the calculated separation efficiency reaches 94.1%. These results indicate that complete separation of the cathode material from the Al foil requires the destruction of the PVDF molecular structure.

The recovery and reuse of TEP solvent significantly enhance the economic and environmental sustainability of the overall process. As shown in Fig. S2a,† the left panel displays a mixed solution of NCM, PVDF binder, and conductive carbon. In the right panel, after centrifugation, a clear phase separation is observed: the bottom layer mainly consists of sedimented NCM material, while the upper layer is the TEP solution, which turns pale yellow due to the presence of PVDF and conductive carbon. TEP solvent can be recovered *via* the non-solvent-induced phase separation method. As shown in the left panel of Fig. S2b,† upon the addition of deionized water to the solvent, a distinct phase separation occurs in the centrifuge tube. PVDF binder loses its solubility in water, aggregates, and encapsulates the conductive carbon, forming a black suspension. After allowing the mixture to stand overnight, the black suspension settles at the bottom of the centrifuge tube, enabling separation and recovery of the TEP solvent. Experimental results show that the recycled TEP solvent can be reused 3–5 times. Additionally, calcination of the black suspension effectively removes the PVDF binder, thereby enabling the recovery of conductive carbon. By comparing the C element content in NCM materials before and after TEP solvent treatment, the separation efficiency of conductive carbon can be estimated. As shown in the XPS spectrum of Fig. S3,† the carbon content in D-NCM decreases from 33.61% to 19.73%, with a corresponding separation efficiency of approximately 36.98%. This further highlights the superiority of the TEP solvent-based separation method.

As shown in Fig. 2e, the mass loss curve of the waste cathode material during calcination exhibits four distinct stages: between 30 and 170 °C, the material loses 6.50% of its

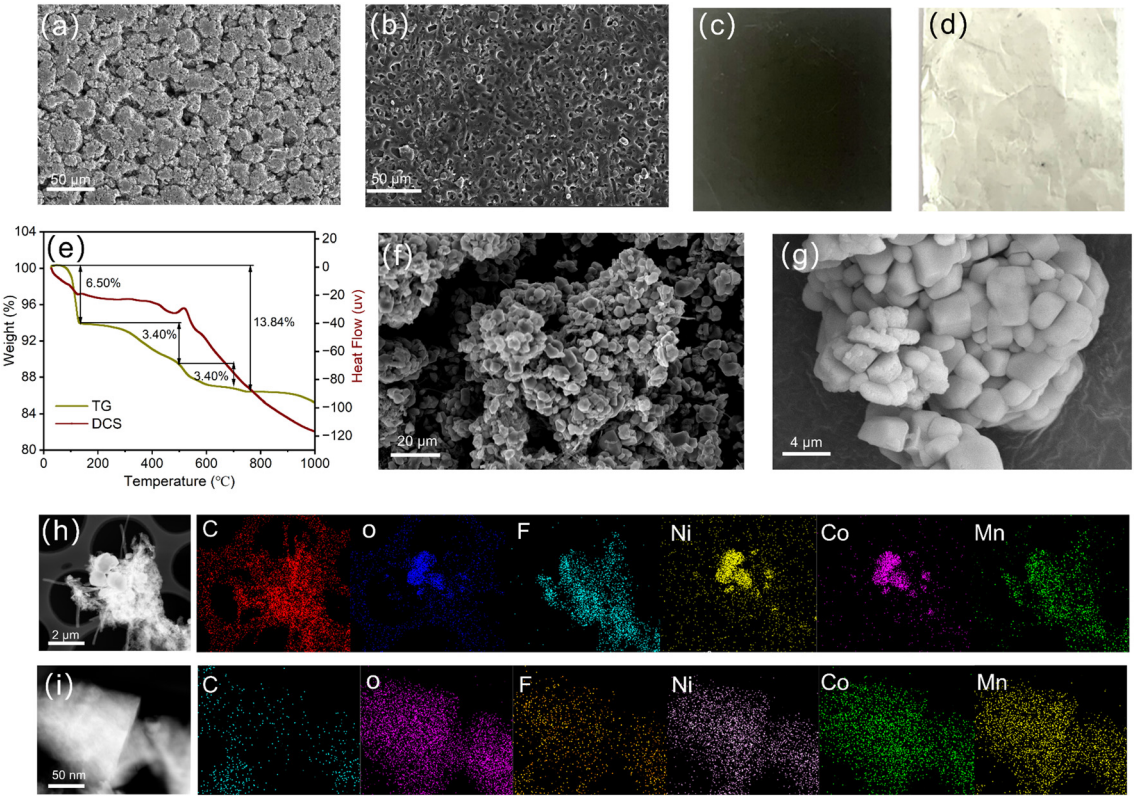

Fig. 2 (a) SEM image of the waste cathode electrode sheet; (b) SEM image of the Al foil after separation; (c) optical images of the S-NCM; (d) optical images of the Al foil; (e) TGA curve of the waste material; (f) SEM image of the S-NCM before separation; (g) SEM image of the regenerated R-NCM; (h) HR-TEM image of S-NCM along with the elemental mapping of C, O, F, Ni, Co, and Mn; (i) HR-TEM image of R-NCM along with the elemental mapping of C, O, F, Ni, Co, and Mn.

mass due to the evaporation of bound water; when the temperature rises to 170 to 500 °C, the thermal decomposition of the PVDF binder results in a 3.40% mass reduction; further increasing the temperature to 500 to 700 °C causes an additional 3.40% loss due to the degradation of the conductive agent; beyond 700 °C, only a slight mass loss of 0.54% is observed, accompanied by the DSC curve leveling off. To verify the structural stability of the NCM material at 850 °C, the study compared the TGA curve of commercial C-NCM (Fig. S4†). C-NCM shows a gradual mass decline between 30 to 1000 °C, with approximately 3% loss occurring in the 30 to 700 °C range, which can be attributed to the decomposition of residual surfactants from the preparation process and the release of lattice oxygen; after 700 °C, its decline trend resembles that of the S-NCM, but the total mass loss reaches 3%, significantly higher than that of S-NCM. This indicates that C-NCM decomposes into stable metal oxide residues at this stage, whereas the slight mass loss of S-NCM is primarily caused by the volatilization of surface lithium salts and the loss of lattice lithium. Combined with literature reports, 850 °C has been confirmed as the optimal temperature to balance regeneration efficiency and structural stability; therefore, this study selected this temperature as the key parameter for the lithium compensation calcination process.

Fig. 2f displays the SEM image of the cathode material S-NCM before separation. The results indicate that the dense structure of the electrode sheet has been disrupted, with the cathode material becoming porous and loosely packed. Additionally, impurities such as PVDF binder and electrolyte residues are visible between the particles. After treatment with TEP solvent, these impurities were effectively removed from the D-NCM sample (Fig. S5†), exposing the secondary particles of the cathode material, which exhibit an irregular block-like morphology.

The spent cathode material was regenerated through high-temperature calcination with the addition of lithium salt. The SEM image of the regenerated R-NCM is shown in Fig. 2g. Compared with S-NCM, the R-NCM retains its irregular block-like morphology, featuring smooth particle surfaces without observable impurities or structural defects. This indicates that the morphological integrity of the material was well preserved throughout the regeneration process. The EDS elemental distribution presented in Fig. 2h and i further reveal changes in the elemental composition. As shown in Fig. 2h, S-NCM exhibits significantly higher C and F content, attributable to the presence of PVDF binder and other residual impurities. In contrast, Fig. 2i reveals that R-NCM is mainly composed of the key cathode elements O, Ni, Co, and Mn, which are uniformly dis-

tributed across the particle surfaces, while the C and F contents are significantly reduced. This confirms the effective removal of PVDF and associated impurities by the TEP solvent. It is worth noting that conventional regeneration methods typically rely on high-temperature calcination to decompose PVDF. However, this process can cause embrittlement of the Al foil, which remains as a contaminant in the regenerated material, thereby increasing the process complexity and economic cost. In contrast, the method employed in this study utilizes TEP solvent to achieve efficient separation of the cathode material from the Al foil without causing corrosion or mechanical damage to the foil. Additionally, it eliminates the negative impact of PVDF residues on the regenerated material, offering a more cost-effective and environmentally sustainable strategy for the green recycling and regeneration of spent LIBs.

3.3 PVDF mechanism of action and failure mechanism

As shown in Fig. 3a, the molecular structure of PVDF contains adjacent CF_2 and CH_2 groups. The highly electronegative F atoms induce strong van der Waals interactions between PVDF chains and attract H atoms from neighbouring molecules forming hydrogen bonds.[29–31] These interactions result in tightly packed and entangled PVDF molecular chains. During the calcination process, the intrinsic structural features of PVDF promote mechanical interlocking between molecular chains, which significantly enhances intermolecular adhesion. When PVDF comes into contact with NCM, van der Waals forces generated by intermolecular interactions lead to strong adhesion between the two materials.[32] As PVDF penetrates into the NCM particles and solidifies, mechanical interlocking at the interface is further reinforced, thereby increasing the overall binding strength. Furthermore, the F atoms in PVDF can form relatively stable interactions with metal oxide ions (*e.g.* Ni^{2+}, Co^{3+}, and Mn^{4+}) on the NCM surface. Furthermore, as illustrated in Fig. 3b, oxygen-containing groups (O^{2-}) on the NCM surface can form hydrogen bonds with the H atoms in PVDF, further improving the interfacial adhesion between PVDF and NCM.[33]

During the charge and discharge processes of LIBs, Li^+ from the electrolyte undergo intercalation and deintercalation reactions on the surface of the Al foil. Meanwhile, other components may also chemically react with the Al foil, altering its surface chemistry and leading to the formation of –OH groups. As illustrated in Fig. 3c, the –OH groups formed on the Al foil surface, due to their high electronegativity, can establish hydrogen bonds with the H atoms in PVDF molecules. Furthermore, the electronegativity difference between the F atoms in PVDF and the –OH groups induce additional van der Waals interactions, enhancing the adhesion between PVDF and the Al foil. In summary, the combined effects of van der Waals forces, hydrogen bonding, and mechanical interlocking among PVDF, NCM, and the Al foil facilitate the strong interfacial adhesion and tight integration of the cathode material with the Al foil. However, these strong interfacial interactions also present significant challenges for the separation of the cathode material from the Al foil during the recycling process.

As shown in Fig. 3d, when TEP solvent comes into contact with PVDF, its high dielectric constant ($\varepsilon \approx 13.5$) matches the solubility parameter of PVDF ($\delta \approx 23$ $MPa^{1/2}$). Under heating conditions, TEP rapidly diffuses and penetrates the PVDF molecular network, disrupting the original molecular chains, causing them to swell and gradually untangle. As shown in Fig. 3e, the failure of the PVDF bonding mechanism results in the formation of pores and cracks at the interface between PVDF and NCM. This disruption causes the hydrogen-bond network between PVDF and NCM to break down, significantly

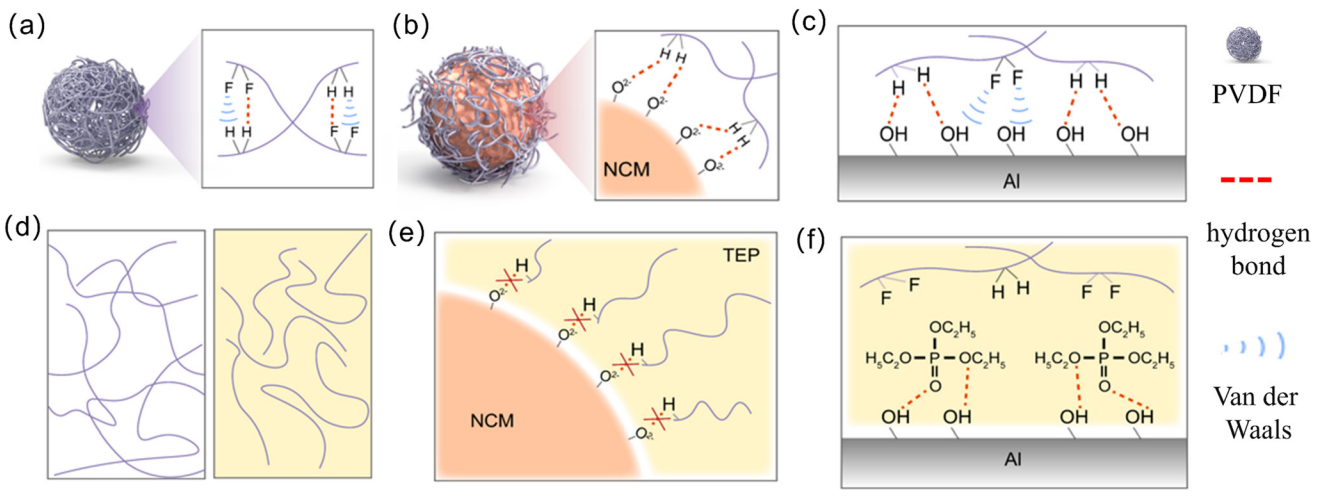

Fig. 3 (a) Mechanical interlocking, hydrogen bonding, and van der Waals forces exist between PVDF molecules; (b) mechanical interlocking, hydrogen bonding, and van der Waals forces between PVDF and NCM; (c) hydrogen bonding and van der Waals forces between PVDF and the –OH groups on the Al foil surface; (d) under the action of TEP solvent, the PVDF molecular chain expands and gradually untangles; (e) under the action of TEP solvent, the hydrogen bond network between PVDF and NCM begins to disintegrate; (f) through the hydrogen bond competition mechanism, TEP and the –OH groups on the Al foil surface preferentially form hydrogen bonds, causing the original hydrogen bonds between PVDF and the –OH groups on the Al foil surface to disappear.

reducing their adhesion strength. According to Table 1, TEP and PVDF share the same hydrogen-bond solubility parameter (δ_h = 9.2), indicating that hydrogen-bond competition is the primary mechanism by which TEP facilitates the delamination of the cathode material from the Al foil. As shown in Fig. 3f, when TEP diffuses to the interface between the cathode material and the Al foil, the P═O and –OC_2H_5 functional groups in TEP molecules act as hydrogen-bond acceptors. These groups form new hydrogen bonds with the H atoms of –OH groups on the Al foil surface, thereby disrupting the original hydrogen bonds between PVDF and the Al foil. This competitive interaction ultimately enables the efficient and selective separation of the cathode material from the Al foil.

To further confirm the structural changes of PVDF, Fig. 4a compares the FTIR spectra of pure PVDF, S-NCM, and D-NCM. The characteristic absorption peaks of PVDF correspond to the bending vibration of CH_2, the symmetric stretching vibration of CF_2, and the out-of-plane bending vibration of CF_2.[34] In the FTIR spectrum of S-NCM, these characteristic peaks are still clearly observed, indicating the presence of residual PVDF in the untreated cathode material. In contrast, these absorption peaks almost completely disappear in the D-NCM spectrum, demonstrating that the molecular structure of PVDF was effectively degraded during the TEP treatment. This structural breakdown significantly reduces the adhesion of PVDF to the Al foil, thereby facilitating the efficient separation of the cathode material. To gain deeper insight into the interactions mechanism between PVDF and TEP, the electrostatic potential (ESP) distributions of both molecules were calculated. As shown in Fig. 4b, the F atoms in the PVDF molecule exhibit a negative electrostatic potential, while the H atoms exhibit a positive potential. This distribution supports the notion that PVDF molecules are primarily stabilized by van der Waals forces and hydrogen bonding, forming a tightly bound structure.[35,36] In contrast, Fig. 4c reveals that the P═O and –OC_2H_5 groups in the TEP molecule exhibit a more negative electrostatic potential than the F atoms in PVDF. This suggests that these functional groups exhibit stronger affinity toward the positively charged H atoms of –OH groups on the Al foil surface.[37,38]

Fig. 4d and e illustrate the hydrogen bond structures and adsorption energy analyses based on DFT calculations. The structural optimization results indicate that –OH groups can be stably adsorbed on the Al (111) surface. As shown in Fig. 4d, the hydrogen bonds formed between the surface –OH groups on the Al foil and PVDF molecules are relatively weak, with bond lengths of 2.202 Å and 2.243 Å, respectively. In contrast, Fig. 4e shows that the hydrogen bonds formed between the same –OH groups and TEP molecules are significantly stronger, with shorter bond lengths of 1.607 Å and 1.959 Å. Furthermore, the adsorption energy between the –OH groups on the Al foil surface and TEP molecules is –1.25 eV, which is significantly more negative than that between the Al –OH groups and PVDF molecules (−0.33 eV), indicating a stronger binding affinity. These DFT results provide further support for the hydrogen bond competition mechanism proposed in the separation process. Specifically, TEP molecules preferentially interact with –OH groups on the Al foil surface, thereby displacing the original PVDF–Al hydrogen bonds and promoting the effective delamination of the cathode material.

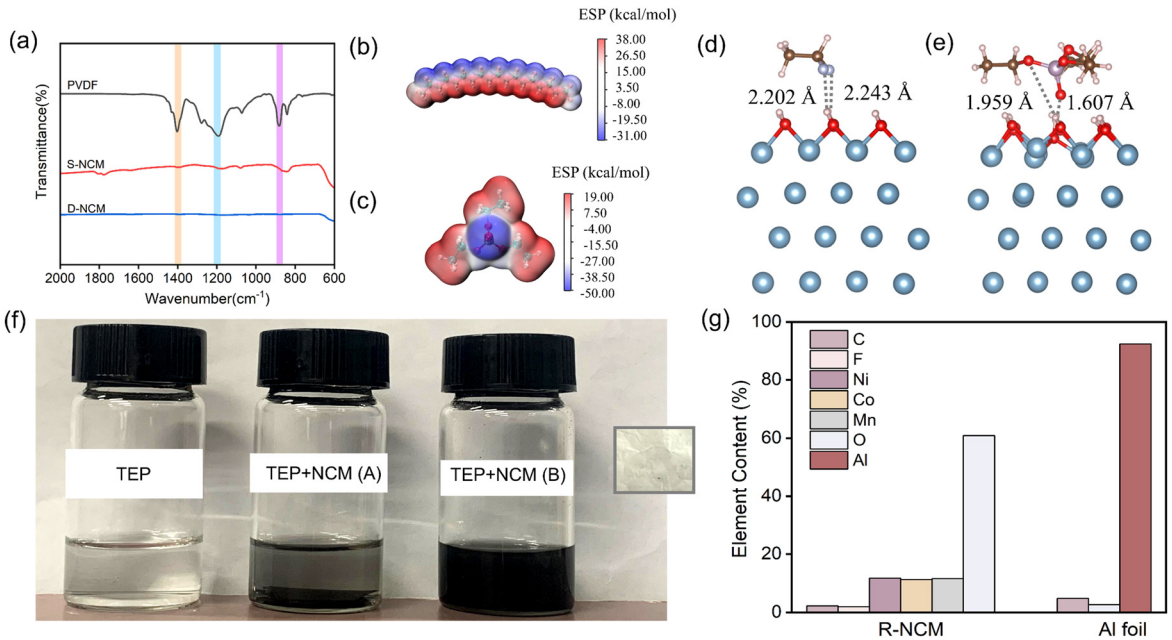

Fig. 4 (a) FTIR spectra of the material; (b) electrostatic potential distribution of PVDF; (c) electrostatic potential distribution of TEP. (d) DFT calculation of adsorption energy between –OH groups on the Al foil surface and PVDF molecules; (e) DFT calculation of adsorption energy between –OH groups on the Al foil surface and TEP molecules; (f) TEP solvent, electrode immersed in TEP solvent (A), fully reacted electrode with TEP solvent (B), and separated Al foil; (g) elemental content analysis of R-NCM and Al foil.

This substantially weakens the adhesion between the cathode material and the Al foil, enabling their efficient separation. As further demonstrated in Fig. 4f, under TEP treatment at 110 °C, the cathode material was successfully separated from the Al foil, with the black cathode powder uniformly dispersed in the solution, further proving the high efficiency of TEP in PVDF removal. Moreover, as illustrated in Fig. 4g, no leaching of transition metal elements was detected on the surface of the recovered Al foil, and the elemental composition of the regenerated cathode material remained unchanged. These results indicates that the TEP-based separation process does not alter the structural composition of the cathode material, ensuring the integrity of its chemical composition and its potential for reuse.

Table 2 compares various methods for separating cathode materials from Al foil. Although mechanical separation is simple in process, it often involves high energy consumption and limited separation efficiency. Solvent-based methods generally exhibit high peeling efficiency; however, they may cause structural damage to the cathode materials or require precise control of solvent composition. In addition, some commonly used solvents (*e.g.*, NMP or H_2SO_4) involve toxic or highly corrosive reagents, posing potential risks to human health and the environment. Pyrolysis can also effectively separate cathode materials, but it is associated with extremely high energy consumption and the release of harmful gases such as HF, leading to considerable environmental pressure. In contrast, the TEP method demonstrates superior environmental friendliness and safety, along with significantly lower energy demand. Under mild conditions (110 °C, 2 h), this method achieves efficient separation while preserving the integrity of the cathode material structure. Furthermore, it features the use of a green solvent, no pollutant emissions, and recyclability of TEP, making it a highly promising, green, and scalable recycling technology for spent lithium-ion batteries.

3.4 Electrochemical performance and characterization of the regenerated material

The primary goal of recycling cathode materials from spent LIBs is to reuse them in the manufacturing of new batteries. However, due to the depletion of Li^+ and the degradation of electrochemical performance, recycled materials require the addition of an appropriate amount of lithium salts for repair and regeneration. In this study, a eutectic molten salt method was employed for lithium supplementation, using LiOH and Li_2CO_3 as lithium sources at a molar ratio of 5.25 : 1.[44] The material was calcined at 450 °C for 5 hours, followed by further heating to 850 °C and an additional calcination for 12 hours to restore the crystal structure.

To evaluate the electrochemical performance of the regenerated materials, a systematic comparison was conducted with the R-NCM and C-NCM. As shown in Fig. 5a, the initial discharge capacities of R-NCM with varying lithium salt additions (1%–9%) were 119.8, 137.5, 143.1, 150.2, 141.2, and 151.5 mAh g^{-1}, respectively, while the corresponding value for C-NCM was 151.5 mAh g^{-1}. With increasing cycle numbers, the discharge capacity of the all samples gradually decreases. After 100 charge–discharge cycles, as shown in Fig. 5b, the discharge

Table 2 Some typical methods for separating cathode materials from Al foil

Methods	Reagent	Separation conditions	Peeling rate	Whether produce HF	Cathode material morphology	Environmentally friendly	Ref.
TEP	TEP	110 °C, 2 h	96.0	No	Complete	Green solvent; no pollution emission; TEP can be recycled	This work
Mechanical separation	—	Grinding miller, 20 s	—	Yes	Complete	High energy consumption; producing HF harmful gases	39
Solvent dissolved	MeOH-CA	45 °C, 15 min	99.5	Yes	Complete	Biodegradable organic acids with no metal loss	15
Solvent dissolved	H_2O, Triton™ X-100, 0.1 M KH_2PO_4	40 °C, 16 min	98.0	—	Complete	The separation process is green and safe; non-toxic waste liquid, and easy to dispose of	17
Solvent dissolved	THF : NMP (50% : 50%)	90 °C,1.5 h	—	Yes	Broken	NMP is harmful to the human body and produces HF harmful gases	40
Solvent dissolved	ChCl : EG(2.3 : 1)	190 °C, 15 min	99.8	—	Complete	The eutectic solvent has low toxicity and mild separation conditions	16
Solvent dissolved	H_2SO_4	135 rpm	—	—	Broken	It is highly corrosive, requires the treatment of a large amount of acidic waste liquid; and there is a risk of contamination in the process	41
Solvent dissolved	2.5 mol L^{-1} H_2SO_4, 20 g/ $LC_2H_2O_4$	85 °C, 100 min	—	Yes	Broken	Organic acids and inorganic acids synergistically enhance leaching; and there are problems of acid waste liquid treatment; low metal selectivity and post-treatment	18
Pyrolysis	—	600 °C	—	Yes	Broken	High energy consumption; the production of HF harmful gases; dust and heat treatment process pollution risk	42
Pyrolysis	—	700 °C, 90 min	100	Yes	—	High energy consumption, the production of HF harmful gases; and the presence of carbon source residues	43

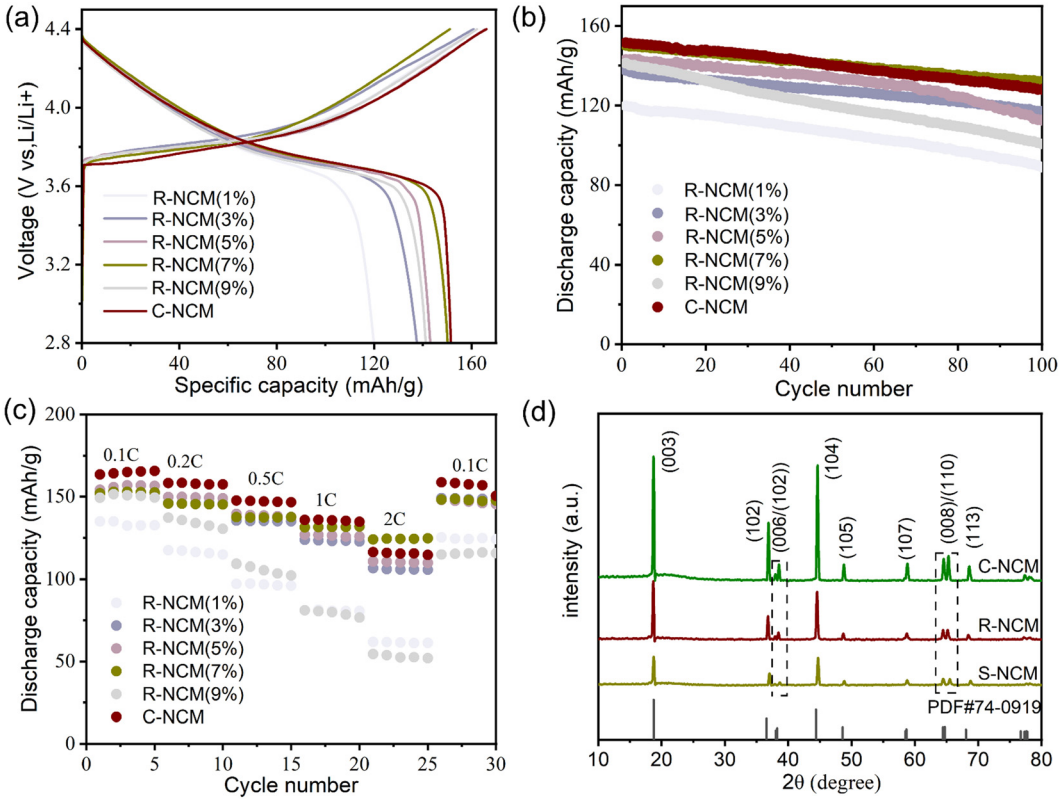

Fig. 5 (a) Initial charge–discharge curves of the samples at 0.5C; (b) performance curves of the samples after 100 cycles; (c) performance curves of the samples after 5 cycles at different current densities; (d) XRD patterns of S-NCM, R-NCM and C-NCM.

capacities of R-NCM (1%–9%) were 88.9, 117.1, 112.7, 132.2, and 100.6 mAh g^{-1}, respectively. Among them, R-NCM with 7% lithium salt exhibited the best cycling stability, achieving a capacity retention of 88.2%, which is comparable to that of C-NCM (129.1 mAh g^{-1}, with a retention of 84.5%). As shown in Fig. 5c, the initial discharge capacities of R-NCM (7%) and C-NCM at 0.1C were 152.1 mAh g^{-1} and 163.5 mAh g^{-1}, respectively. After cycling at varying current densities, the discharge capacities at 0.1C were maintained at 148.2 mAh g^{-1} and 158.8 mAh g^{-1}, respectively, indicating that R-NCM (7%) retained good structural stability and exhibited effective rate capability recovery. Therefore, the optimal electrochemical performance of the regenerated material was achieved with the addition of 7% lithium salt. In Fig. 5d, the XRD patterns of S-NCM, R-NCM and C-NCM both display characteristic diffraction peaks corresponding to the α-$NaFeO_2$-type layered structure with an $R\bar{3}m$ space group. Notably, the diffraction peaks of R-NCM are more intense, sharper, and exhibit a narrower full width at half maximum compared to those of S-NCM, while also showing peak characteristics similar to those of C-NCM, indicating that R-NCM possesses a superior crystal structure and enhanced electrochemical performance.

As shown in Fig. 6a and b present the initial charge–discharge curves and cycling performance of R-NCM and C-NCM were compared. At a current rate of 1C, R-NCM exhibited an initial discharge capacity of 141.4 mAh g^{-1}, with a capacity retention of 86.9% after 100 cycles, which is comparable to C-NCM (143.8 mAh g^{-1}, 89.1%). Fig. 6c shows that R-NCM demonstrates an initial discharge capacity of 154.5 mAh g^{-1} at 0.1C, and after cycling at various current densities, it retains a discharge capacity of 147.9 mAh g^{-1} at 0.1C, similar to C-NCM (163.8 mAh g^{-1} before cycling, 158.8 mAh g^{-1} after cycling). These results indicate that the combination of high-temperature calcination and lithium salt supplementation effectively restores the structural degradation caused by Li^+ depletion during battery operation, improves Li^+ diffusion kinetics, and enables the regenerated material to achieve cycling stability and rate performance on par with commercial cathode materials. As illustrated in Fig. 6d, compared with other experimental methods, the direct regeneration of spent cathode materials using TEP solvent in this work exhibits the best rate performance at both 0.5C and 1C.[39,42,45,46]

To further evaluate the reversibility of R-NCM during cycling, CV tests were performed. As shown in Fig. 6e, the CV curve of S-NCM displays relatively broad and smooth oxidation/reduction peaks, along with a noticeably higher charge voltage. This behaviour can be attributed to the accumulation of surface impurities and the formation of a solid electrolyte interphase (SEI) layer during prolonged cycling.[47,48] In contrast, the CV curves of R-NCM and C-NCM, exhibit nearly overlapping profiles with similar charge/discharge voltage plateaus, indicating that both materials maintain excellent

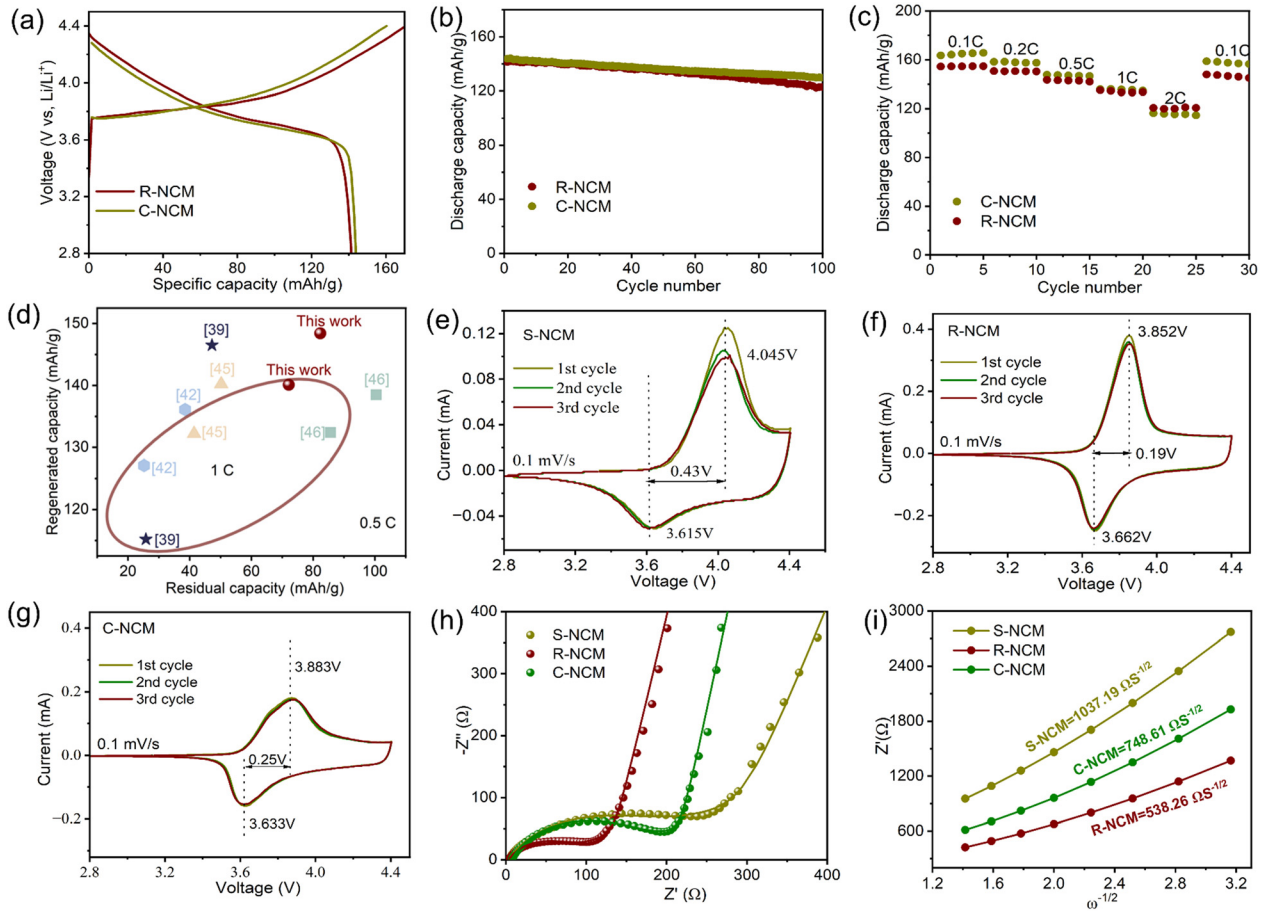

Fig. 6 (a) Initial charge–discharge curves of R-NCM and C-NCM at 1C; (b) performance curves of R-NCM and C-NCM after 100 cycles at 1C; (c) rate performance curves of R-NCM and C-NCM after 5 cycles at different current densities; (d) comparison of rate performance between this work and other reported studies; (e) CV curves of S-NCM after 3 cycles at a scan rate of 0.1 mV s^{-1}; (f) CV curves of R-NCM after 3 cycles at a scan rate of 0.1 mV s^{-1}; (g) CV curves of C-NCM after 3 cycles at a scan rate of 0.1 mV s^{-1}; (h) electrochemical impedance spectra of S-NCM, R-NCM and C-NCM before and after fitting (dots represent raw data, solid lines represent fitted results); (i) corresponding fitted lines of Z' and $\omega^{-1/2}$ for S-NCM, R-NCM and C-NCM.

electrochemical stability during cycling (Fig. 6f and g). To further assess the degree of polarization, the redox peak separation (ΔE) was calculated.[49,50] The ΔE values for S-NCM, R-NCM, and C-NCM are 0.43 V, 0.19 V and 0.25 V, respectively. Among them, S-NCM exhibits the largest ΔE value, indicating the most severe polarization. In comparison, the significantly smaller ΔE of R-NCM indicates lower polarization, suggesting that Li^+ insertion/extraction occurs more smoothly during cycling. This improved kinetic behaviour contributes to the enhanced reversibility and electrochemical performance of the regenerated material.

Fig. 6h shows the EIS of the cathode materials before and after regeneration, as well as that of the commercial material. The semicircle and the intercept with the horizontal axis represent the ohmic resistance (R_s), while the semicircle in the middle frequency range is mainly associated with the interfacial charge transfer resistance (R_{ct}) and the double-layer capacitance (CPE).[51–53] The sloping line at low frequencies is related to the Warburg impedance (σ) associated with Li^+ diffusion. According to the fitting results, the R_{ct} value of S-NCM is 189.9 Ω, while that of R-NCM decreases to 96.22 Ω, which is lower than that of C-NCM (168.01 Ω), indicating a significant improvement in the efficiency of electron transfer from the material to the electrolyte. The linear curve obtained from the fitting of the sloping line is shown in Fig. 6i, where the σ value of R-NCM is 538.26 Ω $S^{-1/2}$, notably lower than that of S-NCM (1037.19 Ω $S^{-1/2}$) and close to that of C-NCM (748.61 Ω $S^{-1/2}$). The Li^+ diffusion coefficients (D_{Li^+}) calculated using eqn (2) and (3) are 1.27 × 10^{-13} cm^2 s^{-1} for S-NCM and 1.54 × 10^{-13} cm^2 s^{-1} for R-NCM, which is clearly higher than that of C-NCM (1.31 × 10^{-13} cm^2 s^{-1}), indicating that R-NCM has a higher Li^+ diffusion coefficient. These results demonstrate that R-NCM exhibits superior structural stability and electrochemical performance compared to S-NCM, consistent with the CV and charge–discharge results discussed earlier.

$$D = \frac{R^2T^2}{2A^2n^4F^4C^4\sigma^2} \quad (2)$$

$$z = R_s + R_{ct} + \sigma\omega^{-1/2} \quad (3)$$

As shown in Fig. 7a, S-NCM exhibits a morphology composed of block-like, rod-like, and sticky structures, with impurity structures originating from residual electrolyte, PVDF binder, and conductive agents that were not completely removed. Further analysis of the TEM image reveals that the S-NCM particles contain multiple impurity structures, and the outermost layer (Region 1) of the particles shows the presence of rock salt-phase NiO and amorphous Li_2CO_3 impurities. The existence of these impurities limits the intercalation and deintercalation of Li^+ during charge and discharge cycles, leading to cation disorder and significantly reducing the material's electrochemical performance. Meanwhile, Region 2 primarily consists of a well-ordered layered structure with an $R\bar{3}m$ space group. The observed lattice fringe spacing of 0.405 nm, corresponding to the (101) crystal plane of $LiNiO_2$ in the standard PDF card. After lithium replenishment, the TEM image of R-NCM shown in Fig. 7b, reveals a significant morphological transformation. The regenerated material retains only irregular block-shaped particles, with no visible impurity structures. Further high-resolution TEM analysis confirms that the crystal structure of R-NCM is more complete, consisting solely of an ordered layered phase. The lattice fringe spacing is measured at 0.266 nm, corresponding to the (015) crystal plane of $LiNiO_2$, indicating improved crystallinity. This structural restoration is primarily attributed to lithium salt supplementation and the thermal decomposition of surface impurities during high-temperature calcination. During this process, Li^+ reoccupies the Li (3a) site, while Ni^{2+} returns to the TM (3b) site, which significantly reduces the cation disorder. Ultimately, the disordered layered structure is effectively eliminated, and the crystal structure is successfully repaired and reconstructed, resulting in a highly ordered layered structure and enhanced electrochemical performance in the regenerated material.

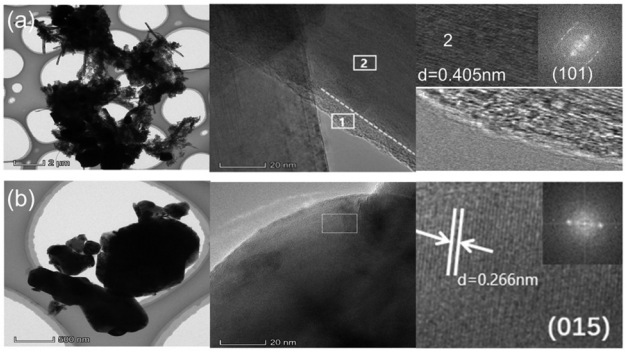

Fig. 7 (a) TEM image of S-NCM; (b) TEM image of R-NCM.

Fig. 8a and b presents the original and fitted XPS data of S-NCM, R-NCM and C-NCM. As shown in Fig. 8a, the Li 1s spectra display two characteristic peaks at 56.0 eV and 54.5 eV, corresponding to Li–F and Li–O, respectively. In S-NCM, the Li–F and Li–O contents are 62.1% and 37.9%, whereas in R-NCM, after lithium supplementation *via* the eutectic molten salt method, the Li–F content decreases to 36.4%, while the Li–O content significantly increases to 63.6%, which is close to that of C-NCM (62.7%). This notable increase in Li–O confirms the successful incorporation of lithium salts into the crystal structure, thereby enhancing the material's electrochemical

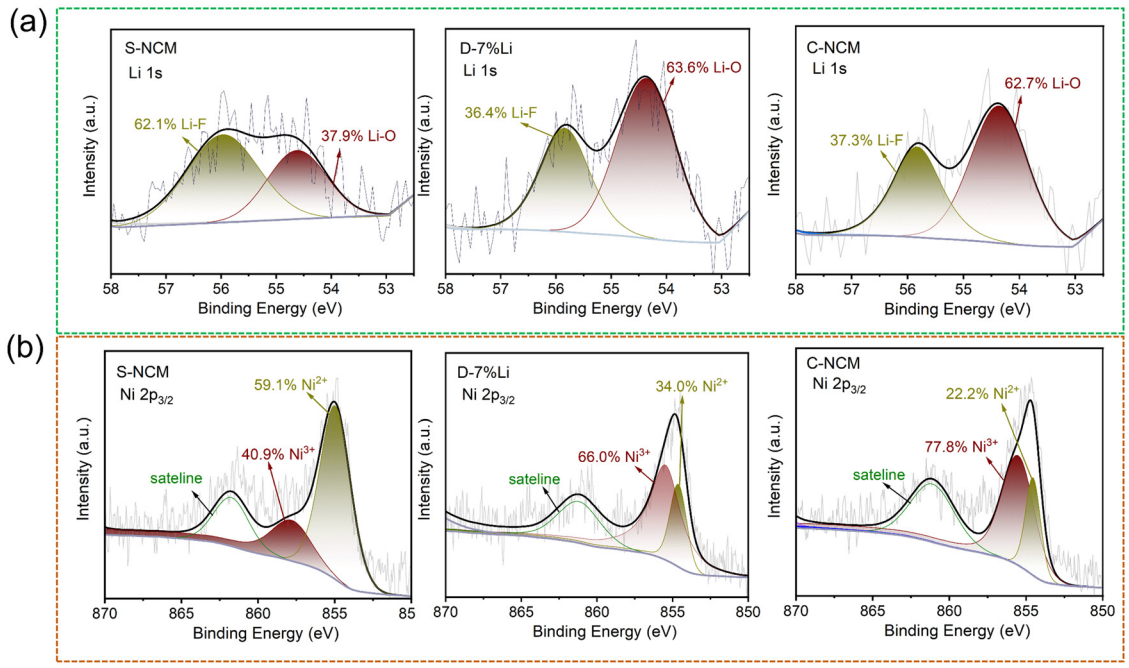

Fig. 8 (a) XPS spectrum and fitting results of Li 1s in the material; (b) XPS spectrum and fitting results of Ni $2p_{3/2}$ in the material.

stability. As shown in Fig. 8b, the Ni $2p_{3/2}$ spectra exhibit fitted peaks at 857.2 eV and 854.8 eV, corresponding to Ni^{3+} and Ni^{2+}, respectively. Compared to S-NCM, the Ni^{3+} content in R-NCM increases markedly from 40.9% to 66.0%, while the Ni^{2+} content decreases from 59.1% to 34.0%, which is close to that of C-NCM (77.8% and 22.2%, respectively). The reduction in Ni^{2+} indicates a more thorough phase transformation from the spinel phase to the layered phase after regeneration *via* the molten salt method, enhancing the structural order of the material. Moreover, the Ni^{3+}/Ni^{2+} ratio is directly related to the degree of cation mixing in layered cathode materials. A higher ratio reflects reduced Ni^{2+} occupancy in the Li layer and a more ordered layered structure. Clearly, R-NCM exhibits a lower degree of cation mixing compared to S-NCM, which contributes to its enhanced structural integrity and superior electrochemical performance.

4. Conclusions

This study proposes an efficient and sustainable TEP-based solvent approach for cathode material separation. To elucidate the underlying separation mechanism, we systematically investigated the intermolecular interactions within PVDF, as well as its adhesion to NCM and the Al current collector. DFT calculations revealed that the adsorption energy of TEP on the Al surface –OH groups (−1.25 eV) is significantly higher than that of PVDF (−0.33 eV), indicating that TEP can competitively displace PVDF *via* stronger hydrogen bonding interactions. Furthermore, the high dielectric constant of TEP, along with its well-matched solubility parameters with PVDF, facilitates polymer chain expansion and disentanglement, thereby weakening the adhesion between NCM and the PVDF binder. Through these two synergistic mechanisms, TEP enables highly efficient cathode material separation, achieving a separation efficiency of 94.1%. Following lithium replenishment *via* the eutectic molten salt method, the electrochemical performance of the regenerated cathode material is effectively restored. At a current density of 1C, the repaired material exhibited a discharge capacity of 141.4 mAh g^{-1}, with a capacity retention of 86.9% after 100 cycles, comparable to that of commercial cathode materials (143.8 mAh g^{-1}, 89.1%). Beyond its high separation efficiency, the TEP-based solvent method also offers significant environmental and economic advantages. Unlike conventional approaches, this method eliminates the need for acidic or alkaline solvents and additional thermal treatments to remove PVDF binders and conductive agents, further enhancing the overall cost-effectiveness of the process. Therefore, this strategy not only provides a viable solution for the sustainable recycling of spent cathode materials but also lays a solid foundation for the development of next-generation LIBs recycling technologies.

Author contributions

Liying Ou: writing – original draft (equal), writing – reviewing and editing (equal); conceptualization (equal), Ying Zhang: conceptualization (equal), writing – original draft (equal), writing – reviewing and editing (equal); Pengwei Li: supervision (equal), writing – reviewing and editing (supporting); Kai Zhu: writing – reviewing and editing (supporting), formal analysis (equal); Yinyi Gao: writing – reviewing and editing (supporting); formal analysis (equal); Dianxue Cao: supervision (equal); conceptualization (lead), writing – reviewing and editing (supporting).

Conflicts of interest

There are no conflicts to declare.

Data availability

The authors confirm that the data of this work are available within the manuscript and its ESI.†

Acknowledgements

This work was supported by Heilongjiang Province Execellent Youth Project Fund (YQ2024B008) and Fundamental Research Funds for the Central Universities (3072025CFJ1004).

References

1 L. Yu, X. Liu, S. Feng, S. Jia, Y. Zhang, J. Zhu, W. Tang, J. Wang and J. Gong, *Chem. Eng. J.*, 2023, **476**, 146733.
2 A. Abdalla, M. Abdullah, M. Dawood, B. Wei, Y. Subramanian, A. Azad, S. Nourin, S. Afroze, J. Taweekun and A. Azad, *J. Energy Storage*, 2023, **67**, 107551.
3 M. Chen, X. Ma, B. Chen, R. Arsenault, P. Karlson, N. Simon and Y. Wang, *Joule*, 2019, **3**, 2622–2646.
4 G. Harper, R. Sommerville, E. Kendrick, L. Driscoll, P. Slater, R. Stolkin, A. Walton, P. Christensen, O. Heidrich, S. Lambert, A. Abbott, K. Ryder, L. Gaines and P. Anderson, *Nature*, 2019, **575**, 75–86.
5 Y. S. Lee, W. K. Shin, A. G. Kannan, S. M. Koo and D. W. Kim, *ACS Appl. Mater. Interfaces*, 2015, **7**, 13944–13951.
6 Z. Yang, H. Huang and F. Lin, *Adv. Energy Mater.*, 2022, **12**, 2200383.
7 R. E. Ciez, R. E. Ciez and J. F. Whitacre, *Nat. Sustainability*, 2019, **2**, 148–156.
8 E. Fan, L. Li, Z. Wang, J. Lin, Y. Huang, Y. Yao, R. Chen and F. Wu, *Chem. Rev.*, 2020, **120**, 7020–7063.
9 Y. Shi, M. Zhang, Y. S. Meng and Z. Chen, *Adv. Energy Mater.*, 2019, **9**, 1900454.
10 D. Song, X. Wang, H. Nie, H. Shi, D. Wang, F. Guo, X. Shi and L. Zhang, *J. Power Sources*, 2014, **249**, 137–141.
11 X. Zhang, Q. Xue, L. Li, E. Fan, F. Wu and R. Chen, *ACS Sustainable Chem. Eng.*, 2016, **4**, 7041–7049.

12 X. Zeng, J. Li and L. Liu, *Renewable Sustainable Energy Rev.*, 2015, **52**, 1759–1767.
13 A. Pavlovskii, K. Pushnitsa, A. Kosenko, P. Novikov and A. Popovich, *Inorganics*, 2022, **10**, 141.
14 Y. Ji, C. Jafvert, N. Zyaykina and F. Zhao, *J. Cleaner Prod.*, 2022, **367**, 133112.
15 Y. Han, M. Yan, Y. Fang, Y. Xiong, Y. Wang, Y. Chen, L. Lin, J. Qian, T. Mei and X. Wang, *J. Power Sources*, 2024, **603**, 234417.
16 M. Wang, Q. Tan, L. Liu and J. Li, *J. Hazard. Mater.*, 2019, **380**, 120846.
17 Y. Bai, L. Yu and I. Belharouak, *J. Power Sources*, 2024, **592**, 233954.
18 C. Yang, J. Wang, P. Yang, Y. He, S. Wang, P. Zhao and H. Wang, *Sustainability*, 2022, **14**, 14169.
19 Y. Bai, R. Essehli, C. Jafta, K. Livingston and I. Belharouak, *ACS Sustainable Chem. Eng.*, 2021, **9**, 6048–6055.
20 G. Kresse and J. Furthmüller, *Comput. Mater. Sci.*, 1996, **6**, 15–50.
21 M. Segall, J. Philip, M. Probert, C. Pickard, P. Hasnip, S. Clark and M. Payne, *J. Phys.: Condens. Matter*, 2002, **14**, 2717.
22 P. Blöchl, *Phys. Rev. B: Condens. Matter Mater. Phys.*, 1994, **50**, 17953–17979.
23 J. Perdew, K. Burke and M. Ernzerhof, *Phys. Rev. Lett.*, 1996, **77**, 3865–3868.
24 S. Jung, H. Gwon, J. Hong, K. Park, D. Seo, H. Kim, J. Hyun, W. Yang and K. Kang, *Adv. Energy Mater.*, 2014, **4**, 1300787.
25 Y. Chen, Y. Zhang, B. Chen, Z. Wang and C. Lu, *J. Power Sources*, 2014, **256**, 20–27.
26 H. Zhou, F. Xin, B. Pei and M. S. Whittingham, *ACS Energy Lett.*, 2019, **4**, 1902–1906.
27 L. Mu, R. Lin, R. Xu, L. Han, S. Xia, D. Sokaras, J. Steiner, T. Weng, D. Nordlund, M. Doeff, Y. Liu, K. Zhao, H. Xin and F. Lin, *Nano Lett.*, 2018, **18**, 3241–3249.
28 Y. Bai, N. Muralidharan, J. Li, R. Essehli and I. Belharouak, *ChemSusChem*, 2020, **13**, 5664–5670.
29 L. Zhao, Z. Sun, H. Zhang, Y. Li, Y. Mo, F. Yu and Y. Chen, *RSC Adv.*, 2020, **10**, 29362–29372.
30 H. Wang, J. Liu, X. Bai, S. Wang, D. Yang, Y. Fu and Y. He, *Waste Manage.*, 2019, **91**, 89–98.
31 Y. Ma, J. Ma and G. Cui, *Energy Storage Mater.*, 2019, **20**, 146–175.
32 L. He, S. Sun, X. Song and J. Yu, *Waste Manage.*, 2015, **46**, 523–528.
33 X. Zhong, J. Han, L. Chen, W. Liu, F. Jiao, H. Zhu and W. Qin, *Appl. Surf. Sci.*, 2021, **553**, 149564.
34 S. Gu, G. He, X. Wu, Z. Hu, L. Wang, G. Xiao and L. Peng, *J. Appl. Polym. Sci.*, 2010, **116**, 852–860.
35 P. Xu, D. Tan, B. Jiao, H. Gao, X. Yu and Z. Chen, *Adv. Funct. Mater.*, 2023, **33**, 2213168.
36 Y. Bai, W. B. Hawley, C. J. Jafta, N. Muralidharan, B. J. Polzin and I. Belharouak, *Sustainable Mater. Technol.*, 2020, **25**, e00202.
37 X. Chen, S. Li, X. Wu, T. Zhou and H. Ma, *J. Cleaner Prod.*, 2020, **258**, 120943.
38 K. He, Z. Zhang, L. Alai and F. Zhang, *J. Hazard. Mater.*, 2019, **375**, 43–51.
39 L. Wang, H. Deng, Y. Chen, M. Zhang, J. Li, C. Yang, L. Yang, X. Luo, L. Zhou, Z. Li and X. Kong, *Surf. Interfaces*, 2025, **62**, 106126.
40 A. Sarkar, R. May, S. Ramesh, W. Chang and L. Marbella, *ChemistryOpen*, 2021, **10**, 545–552.
41 G. Shi, N. Zhang, J. Cheng, S. Zhang, X. Shao, L. Wen, X. Chen and B. Xin, *J. Environ. Chem. Eng.*, 2023, **11**, 111207.
42 X. Meng, J. Hao, H. Cao, X. Lin, P. Ning, X. Zheng, J. Chang, X. Zhang, B. Wang and Z. Sun, *Waste Manage.*, 2019, **84**, 54–63.
43 G. Lombardo, B. Ebin, M. Foreman, B. Steenari and M. Petranikova, *ACS Sustainable Chem. Eng.*, 2019, **7**, 13668–13679.
44 S. Jin, J. Liang, D. Mu, T. Lin, Y. Tian, J. Zhang, Y. Wang, M. Chen, Q. Shi and C. Dai, *SusMat*, 2023, **3**, 362–378.
45 J. Hu, C. Li, X. Wang, J. Yuan, Y. Zhang, D. Chen, G. Li, A. Guo and L. Zhao, *Mater. Today Commun.*, 2024, **38**, 108449.
46 H. Song, Z. Zhang, L. Zhang, W. Dong, Y. Ding, Z. Wang, H. Wang, H. Deng and Q. Cheng, *Ionics*, 2023, **29**, 3543–3547.
47 Y. Xi, Y. Liu, D. Zhang, S. Jin, R. Zhang and M. Jin, *Solid State Ionics*, 2018, **327**, 27–31.
48 Z. Chen, Y. Liu, Z. Lu, R. Hu, J. Cui, H. Xu, Y. Ouyang, Y. Zhang and M. Zhu, *J. Alloys Compd.*, 2019, **803**, 71–79.
49 G. Song, H. Zhong, Z. Wang, Y. Dai, X. Zhou and J. Yang, *ACS Appl. Energy Mater.*, 2019, **2**, 7923–7932.
50 B. Chu, S. Liu, L. You, D. Liu, T. Huang, Y. Li and A. Yu, *ACS Sustainable Chem. Eng.*, 2020, **8**, 3082–3090.
51 L. Nie, Z. Wang, X. Zhao, S. Chen, Y. He, H. Zhao, T. Gao, Y. Zhang, L. Dong, F. Kim, Y. Yu and W. Liu, *Nano Lett.*, 2021, **21**, 8370–8377.
52 L. Yao, F. Liang, J. Jin, B. V. R. Chowdari, J. Yang and Z. Wen, *Chem. Eng. J.*, 2020, **389**, 124403.
53 P. Yue, Z. Wang, X. Li, X. Xiong, J. Wang, X. Wu and H. Guo, *Electrochim. Acta*, 2013, **95**, 112–118.

